

Giant Rashba spin splitting with unconventional spin texture in a quantum spin hall insulator

C. Mera Acosta,^{1,*} O. Babilonia,¹ L. B. Abdalla,¹ and A. Fazzio^{1,†}

¹*Instituto de Física, Universidade de São Paulo, CP 66318, 05315-970, São Paulo, SP, Brazil*

(Dated: August 20, 2015)

The main objective of spintronics is to understand the mechanisms by which it is possible to achieve efficient electrical control of spin configurations and of spin currents[1, 2]. In the last decade, the way to achieve this objective has experienced a breakthrough, due to: *i*) the discovery and understanding of a mechanism to generate spin currents in conductors with magnetic order and in paramagnetic conductors/semiconductors[3–5], *ii*) the experimental observation of theoretically proposed spin injector systems[1, 6, 7] and *iii*) the synthesis of 2D materials with long spin relaxation time[1, 8]. The generation of spin currents, spin injections and spin conservation are mediated by the Spin-Orbit Coupling (SOC) mainly via topological effects and/or Rashba effect[9–11]. Thus, the search for systems experiencing these properties is a primary concern for the development in spintronics. In this work, we propose a non-centrosymmetric honeycomb-lattice quantum spin hall effect family formed by atoms of the groups IV, V and VII of the periodic table, as shown in Fig1a. We made a structural analysis and a Z_2 characterization. This material presents a giant Rashba-type spin-splitting with an unusual spin texture and a hexagonal warping effect, which lead to scattering process different from the usual materials with non-trivial topological phases. We proposed a four band effective model to explain both the origins of such unusual spin texture in the Rashba effect and the SOC band inversion in the topological insulator phase. This dual behavior only has been reported in the BiTeI 3D topological insulator[12, 13].

Topological insulator materials support helical metallic edge states (or surface states for 3D systems), forming topological Dirac fermions protected by the time-reversal symmetry on an insulating bulk[6, 7]. This topological protection is responsible for the absence of backscattering process as well as the in-plane chiral spin texture in this metallic states. This particular edge band dispersion and spin helicity have been experimentally characterized via Angle-Resolved Photoemission Spectroscopy (ARPES) and localized Scanning Tunneling Microscope (STM) transport measurements[6, 14]. On the other hand, the Rashba SOC leads to parallel spin-polarized

band dispersion curves with in-plane opposite helical spin texture[15], allowing the control of the spin direction through an electric field[9]. This interaction originates from the lack of spatial inversion symmetry along the perpendicular direction to a two-dimensional electron gas (2DEG), which is hosted on the surface of a system or on an interface. The dispersion curves and Fermi contours have been characterized by spectroscopic measurements for many surfaces[16–18] and interfaces[19]. Large Rashba couplings are found in materials formed by heavy elements with strong intrinsic SOC such as Bi, Pb, W and others[19–23].

The intense study of the nontrivial topological phase in condensed matter systems began with the theoretical proposal of the quantum spin Hall effect in graphene[24]. Despite its small SOC gap, this honeycomb-lattice material has promoted several searches for new materials with the same electronic and structural properties[25–32]. Several graphene-like materials proposed theoretically have been synthesized. However, most of these systems, different from the quantum wells, have direct band gap in the K point of the Brillouin Zone (BZ). Therefore, the sub-lattice symmetry breaking bring the system to a trivial band gap, this effect can easily arise when the deposition on a substrate is considered. The functionalization of germanene [33] and tin monolayers [28], which exhibit a non-trivial band gap located in the Γ point, motivated us to search honeycomb-lattice systems with strong SOC and band gap located at this point.

Geometry and electronic properties: We propose a system with a honeycomb lattice formed by atoms of the groups IV, V and VII of the periodic table, as shown in Fig1a. Interpreting the hexagonal lattice as two triangular sub-lattices A and B, the system has a V atom type on the sub-lattice A, whereas in the sub-lattice B it has a IV-VII dimer. These non-centrosymmetry systems have a buckled format and fulfill the symmetry operations of the C_{3v} point group symmetry. From the *ab initio* calculations of the phonon spectrum for this family of materials, we find that the system formed by Bi, Pb and I atoms is mechanically stable. The formation energy is about -0.77 eV, which is calculated as: $E_F = E_{\text{PbBiI}} - \mu_{\text{Pb}} - \mu_{\text{Bi}} - \mu_{\text{I}}$, where E_{PbBiI} is the energy of the system, and $\mu_{\text{Pb,Bi,I}}$ are the chemical potential from the respective bulk phase.

In Fig 1, we present the band structure and the projections of the wave function in the p_z and $p_{x,y}$ atomic

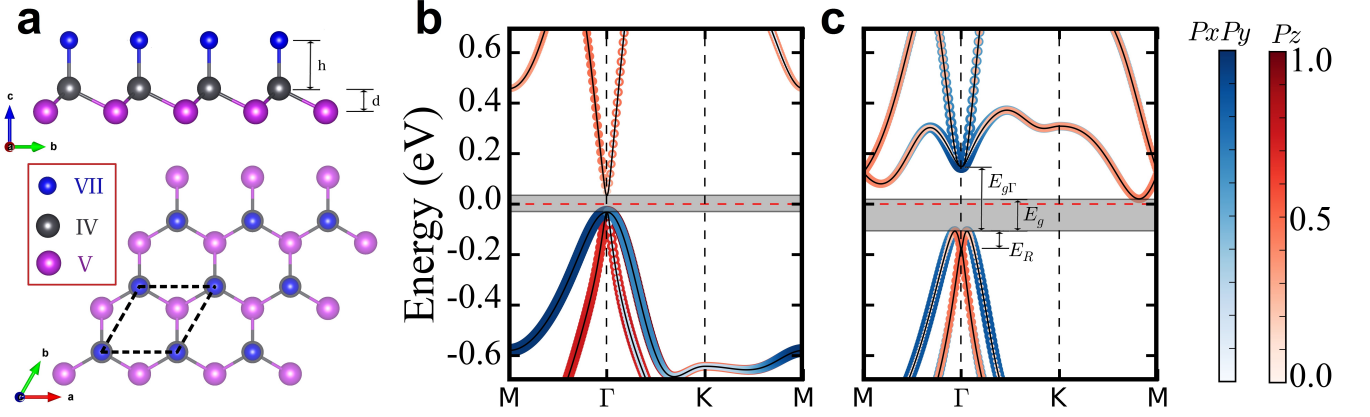


Figure 1. Side and top view of the atomic structure of PbBiI (a), and Band structure with SOC (b) and without SOC (c). The projection in the $p_x + p_y$ orbitals of all atoms are indicated by the blue circles, while the Se p_z orbitals are indicated by the red circles. Both color are in gradient scale depending on weight of that projection in each state.

orbitals for each band and \mathbf{k} -point, for both cases taking into account and disregarding the SOC. First, we will discuss the band structure and the atomic orbitals interaction disregarding the SOC. We find that the system is a direct gap semiconductor. The valence band maximum and the conduction band minimum are located in the gamma point. Since the system has no magnetic moment, the Time Reversal (TR) symmetry is preserved and the spin components are bi-degenerate, as shown in Fig 1b. The valence orbitals of IV, V and VI atoms are mainly p -type orbitals, these orbitals are responsible for the chemical bonds. The crystal has a layered structure, so the z direction is different from the x or y directions in the atomic plane. Thus, there is an energy splitting between p_z and $p_{x,y}$ orbitals. We find that the band structure near the Fermi energy is described by p -type Bi atomic orbitals. For Bi atom the $p_{x,y}$ orbitals have lower energy than p_z orbitals. Consequently before SOC is considered, the conduction band mainly consists of p_z Bi orbitals, whereas the valence band is dominated by the $p_{x,y}$ Bi orbitals.

Next we include SOC effect in the above atomic picture. The atomic SOC Hamiltonian is given by $H_{so} = \lambda \mathbf{S} \cdot \mathbf{L}$ with $\lambda = \frac{1}{2m_0^2 c^2 r} \frac{\partial U}{\partial r}$ depending on the detailed potential U of atoms, which couples orbital angular momentum to spin[34]. From the symmetry properties and how this Hamiltonian modify the atomic spectrum of Bi, Pb and I atoms in the crystal, we find that the spectrum energy at the Γ point is given by the $\{|\Lambda_J, j_z\rangle\}$ effective states. J is the effective total angular momentum with projection j_z in the z axes and Λ corresponding to the Bi and Pb-I contributions. Transforming the p_x and p_y orbitals to p_{\pm} with definite orbital angular momentum, we have $J = 3/2, 1/2$ and $j_z = \pm 3/2, \pm 1/2$. The $|\Lambda_{3/2}, \pm 3/2\rangle$ effective states are associated with the p_+ and p_- effective orbitals, whereas the $|\Lambda_J, \pm 1/2\rangle$ effective states are linear combinations of p orbitals, in this

case mainly of p_z orbitals. Thus, as shown in Fig 1c, at the Γ point, the character of the band structure is inverted, the conduction band mainly consists of $p_{x,y}$ Bi orbitals while the valence band is dominated by the p_z Bi orbitals. The inclusion of the SOC change the gap direction and the band structure is highly modified. The valence band maximum is located in the $\Gamma \rightarrow K$ direction very close to the Γ point and the conduction band minimum is located in the $M \rightarrow K$, as shown in Fig 1c. We classify the SOC effects in the band structure into two classes: *i*) at the time reversal invariant momenta such as Γ and M the degeneracy remains. Far from these points, the spin degeneracy is lifted and the M-shape associated with the Rashba effect appears in the valence bands. This effect is characterized by the energy splitting, E_R , represented in the Fig 1c; *ii*) by turning the strength of the SOC, λ_{SOC} , where $\lambda_{SOC} = 0(1)$ means absence (full presence) of SOC, we verify that at the Γ point a topological phase transition occurs. The system pass through a metal state with $\lambda_{SOC} = 0.65$, showing a band inversion characterized by energy gap at the Γ point, $E_{g\Gamma}$, which it is not always equal to the band gap of the system E_g . Later, we will discuss both Rashba effect and topological properties in the PbBiI system.

In the lowest energy configuration, the Bi-Pb and Pb-I (h) bonds have 3.04 Å and 1.35 Å of length, respectively. Whereas, the buckled, d , have 1.3 Å of length. Using GGA functional, we find that the lattice constant is 4.77 Å, whereas for LDA is 4.53 Å, as shown in Fig 2a. We find that the substitution of Pb atoms by Sn atoms or changing the lattice constant allows the control of both the band gap direction (Fig 2b) and the like-Rashba spin-splitting in the valence band (Fig 2c). The decrease (increase) of the lattice constant can be understood as a compressive (tensile) strain. We noticed three different behaviors depending on the intensity of the strain applied: semi-metal, indirect band gap semiconductor and

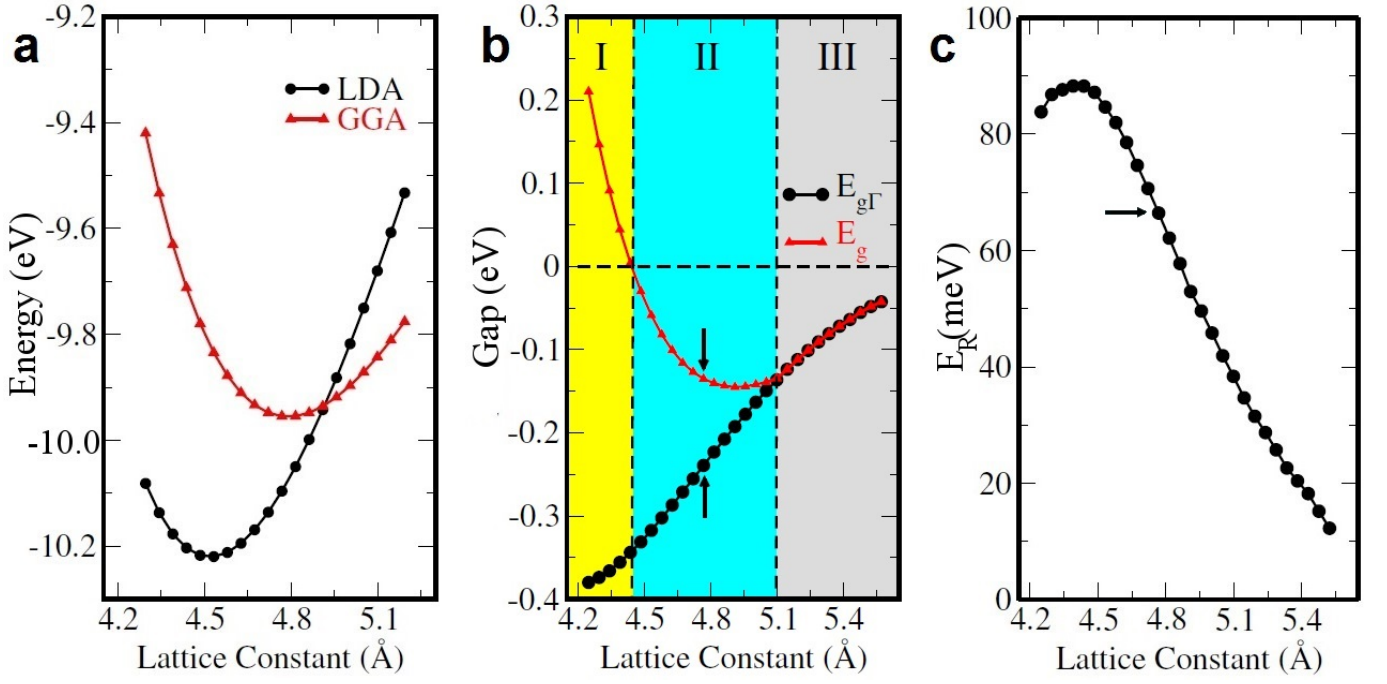


Figure 2. (a) Energy in function of lattice parameter depending on the exchange-correlation functional used, i.e Local Density Approximation (LDA) or Generalized Gradient Approximation (GGA). (b) Gap size in function of lattice parameter, where E_g and $E_{g\Gamma}$ are the gap size of the system and only in the Γ point respectively. The dashed line at 0.0 of the gap represent the value where the variable E_g become inverted. (c) Size of Rashba spin splitting in meV in function of lattice parameter.

direct band gap semiconductor, as represented in Fig 2b by the regions I, II and III, respectively. The equilibrium position is represented by arrows, shown as in the Fig 2. As mentioned above, in the region II, in which the system is in the equilibrium lattice parameter, $E_{g\Gamma}$ is negative indicating a band inversion at the Γ point. The gap $E_{g\Gamma}$ is different from the indirect band gap E_g , which was also considered negative for comparison purposes. In the region I, when we apply compressive strain, the minimum of the conduction band, in $M \rightarrow K$ direction, begins to descend and cross the Fermi energy for $a = 4.3$ Å, forming a semi-metal. To represent this behavior, we change the sign of the band gap E_g . In the region III, we consider a tensile strain, E_g and $E_{g\Gamma}$ are equals and the system behaves as a semiconductor with a direct band gap at the Γ point. For any value of strain, the states near to the Fermi energy in the Γ point remain inverted, so if this band inversion is associated with a topological state, this state will be robust against strain, even for a tension of 20% (5.6 Å), as shown in Fig 2.

Unconventional Rashba effect: According to our calculations, the value of the spin-splitting in the valence band due to the Rashba effect is about 60 meV, which is huge compared with the values found in 2D systems and surprisingly is on the order of the highest found in 3D systems[35]. As mentioned above, this phenomenon is robust to strain, even for large compressive strain, large Rashba values ($E_R = 90$ meV) may be obtained, as

shown in Fig 2c. Although the conduction band does not have the M-shape characteristic of the Rashba effect, the $\langle S_z \rangle$ spin texture evidence the same properties of the systems that exhibit this effect. Specifically, in both valence and conduction bands, the usual $\langle S_z \rangle$ spin texture associated with the Rashba spin-splitting is observed, as represented in Fig 3a. However, the $\langle S_x \rangle$ and $\langle S_y \rangle$ spin components exhibit an unusual behavior. In Fig 3b, we show the in-plane spin texture in six constant energy planes. These planes cut the two conduction bands named CB1 and CB2, and the two valence bands named VB1 and VB2 (see Fig 3a). Near to the Γ point, the VB1 exhibits a clockwise helicity, as shown in the energy plane e1. Far from this point ($|\mathbf{k}|$ greater than 0.1 in the reciprocal space), this helicity switches to counterclockwise. Very close to the Γ point, the VB2 exhibits a counterclockwise helicity. This helicity switches to counterclockwise for k -values greater than 0.01, as is observed in the e2 and e3 energy planes. For BV1 and BV2 the spin texture behaviors can be divided into three regions of the \mathbf{k} -space, $|\mathbf{k}|$ being the norm of the vector $\mathbf{k} = (k_x, k_y)$: *i*) when $|\mathbf{k}|$ is less than 0.01, the spin texture of both bands rotates in the same direction, *ii*) when $|\mathbf{k}|$ is greater than 0.01 and less than 0.1, the bands have the same helicity, unlike the usual behavior in the Rashba effect and *iii*) when k is greater than 0.1, the bands have different helicity. The in-plane spin rotation in the CB1 and CB2 have the same behavior described

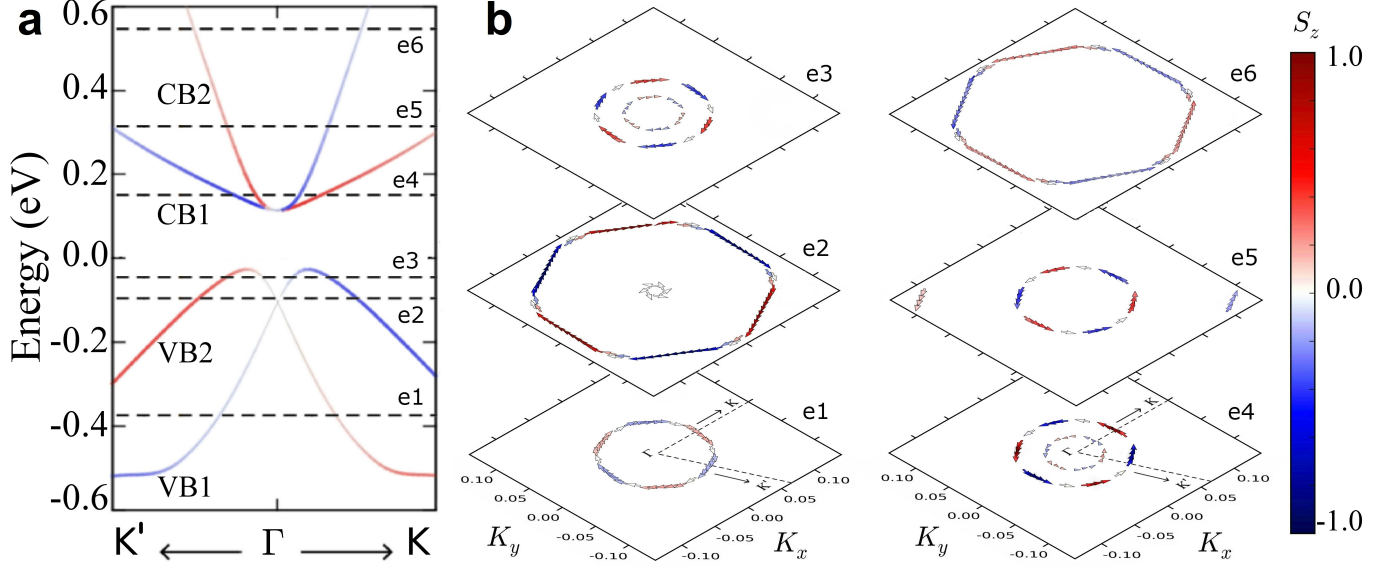


Figure 3. (a) Bandstructure of PbBiI in the direction $K' - \Gamma - K$, with six cut e1 – 6 in constant energy of the valence and conduction bands VB1, VB2, CB1 and CB2 respectively. (b) Spin texture from cuts of the bandstructure e1 – 6. Spin projection in (\hat{x}, \hat{y}) plane are represented by the size of the arrow. For $\langle S_z \rangle$ we used a red-white-blue color gradient scale. In both figures dark red and dark blue represent a $\langle S_z \rangle$ up and down spin configuration respectively.

above. However, the CB1 and CB2 have opposite helicity direction to that found in the VB1 and VB2, as shown in e4, e5 and e6 energy planes in Fig 3b.

We observed a hexagonal modulation of the bulk states analogous to the existence of a nonlinear term in the SOC[36], as shown in the e6 and e2 energy planes in Fig 3b. The nonlinear terms in the SOC lead to higher order components of the Rashba effect[37], which induce this hexagonal warping effect. This modulation is also observed in the surface states of the 3D topological insulators and is associated with the R_3 symmetry breaking[34, 36]. From our knowledge, there are no other 2D systems experiencing this hexagonal warping effect in the bulk states. Additionally, in the spin texture, we observed a periodic $\langle S_z \rangle$ spin precession, which is associated with the lack of space inversion symmetry and the threefold rotation symmetry breaking. Interestingly, although the band structure describes a 2D semiconductor, the $\langle S_z \rangle$ spin polarization increases as the energy increases. Thus, near to the Fermi energy the $\langle S_z \rangle$ spin-polarization is null, the same as occurs in the surface states of Bi₂Te₃[36]. The consequence of these $\langle S_z \rangle$ spin-component fluctuation and hexagonal warping effect in the electronic and transport properties has been extensively studied[36, 38, 39].

In the Rashba effect, at any energy plane, the eigenstate $\psi_n(\mathbf{k})$ has opposite spin direction to the eigenstate $\psi_n(-\mathbf{k})$ with the same band index and opposite momenta. Thus, near to the Fermi energy, the backscattering processes are forbidden. This behavior is also observed in the PbBiI system, as shown in Fig 3. On the

other hand, in the Rashba effect, the inelastic scattering between different bands is possible, i.e, the eigenstate $\psi_n(\mathbf{k})$ has the same spin direction to the eigenstate $\psi_{n'}(-\mathbf{k} + \Delta\mathbf{k})$. Because of the particular in-plane spin texture helicity in the bulk states of the PbBiI system, this scattering process in the PbBiI system is different. As is observed in Fig 3b, except for the small energy range characterized by the e2 energy plane, in order for inelastic scattering processes between different band to occur, the $\langle S_x \rangle$ and $\langle S_y \rangle$ spin flip is necessary. Provided the TR symmetry is preserved, this protection against backscattering will remain. These "TR protected bulk states" has no origin in the topological properties of the system and is only a result of the combination of the effects caused by the high order Rashba components. This will be discussed later through the analysis of each of these components. As far as we know, the PbBiI system is the first system that has such spin texture properties in their bulk band structure. This behavior is of deep interest in spintronics.

Topological insulator phase: We find that in addition to the inherent TR protected bulk states, the PbBiI system is also a 2D topological insulator with 1D TR protected edge states. This topological protection against any TR invariant perturbation, can be seen through the topological order described by the Z_2 invariant [24, 40–42]. Thus, in order to fully determine the topological character of the non-centrosymmetric PbBiI system, we implemented the evolution of Wannier Center of Charges (WCCs) as an alternative method for the Z_2 invariant calculation using *ab-initio* simulations (see methods). In

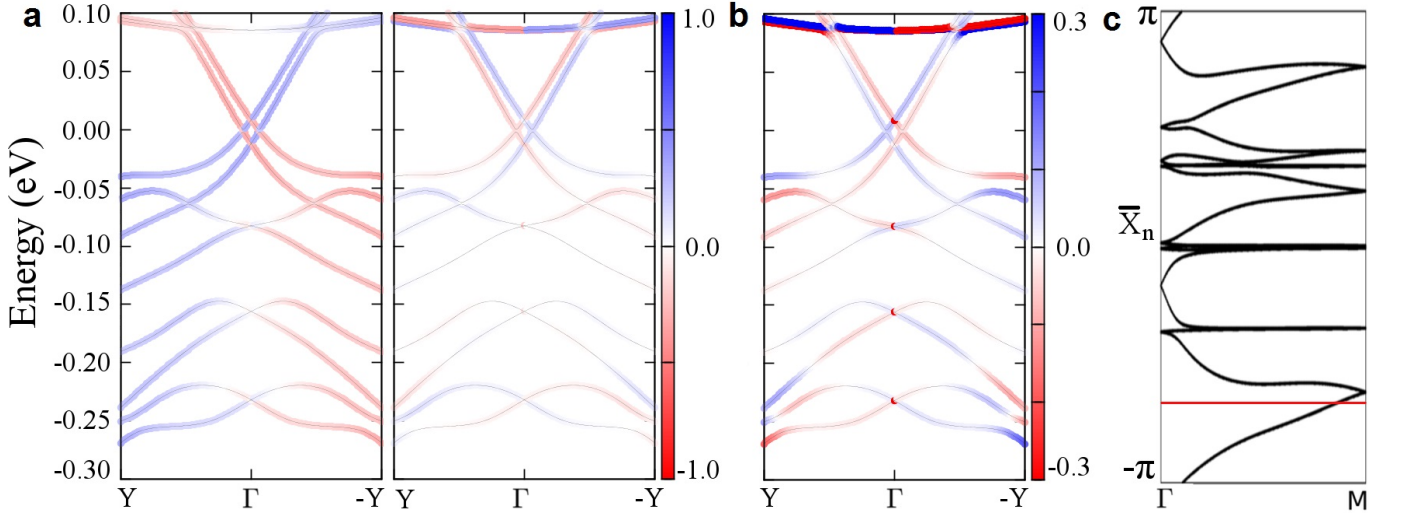


Figure 4. Spin texture band structure of armchair nanoribbon of the system PbBiI with the $\langle S_x \rangle$ (a) left, $\langle S_y \rangle$ (a) right, $\langle S_z \rangle$ (b) spin components projection. The width of the calculated ribbon is 98.7 Ån (c) we have the evolution of Wannier Center of Charges, and if we draw an horizontal line of reference that cross the picture, we would have at least an odd number of crossing, showing that this material is a topological insulator.

Fig 4c, we show that there is no a horizontal reference line that cross the evolution of the WCCs at least an odd number of times, showing that this material is a topological insulator[43].

Using electronic structure calculations, we verify that the band structure of a nanoribbon of the PbBiI system exhibits edge states in the middle of the bulk band gap, regardless of the nanoribbon orientation. In Fig 4b, we present the spin texture in the band structure of an Armchair nano-ribbon, which has two Dirac cones in the Γ point formed by bands with opposite spin, as expected. When the nano-ribbon is constructed, the mirror symmetry is broken and therefore, the Dirac cones located at different edges are nondegenerate. As shown in the Fig 4, although the edges states satisfy the TR symmetry and have the chiral spin helicity, the spin has preferentially the k_x direction. The S_y and S_z spin components are lower for both bulk states and metallic edge states. We find that in the nanoribbon band structure, the protected bulk states are maintained, but now these are unidirectional. Thus, in the nanoribbon, the backscattering is forbidden for both edge conductivity channels and bulk conductivity channels. This suggests that, contrary to what happens in most systems with nontrivial topological phases, the bulk states would not pose a problem for spintronic devices.

Model: In order to understand both topological properties and unconventional spin texture in the Rashba effect, we propose a simple model that captures the electronic properties near to the Fermi energy. Because the valence and conduction bands are formed mainly by the effective states $\{|\text{Bi}_J, j_z\rangle\}$ with $J = 3/2, 1/2$, we use these

states to form the basis of our model. By construction, this base contains intrinsically the full SOC. From a phenomenological analysis of the electronic structure, we initially describe the effects, in principle, required to reproduce the results obtained via DFT calculations. Subsequently, using symmetry elements, we construct a tight-binding effective model, showing that these effects arise naturally when the $\mathbf{k} \rightarrow \Gamma$ limit is considered.

Although, the Rashba effect and the surface states in 3D topological insulators arise as a result of different physical properties, the effective Hamiltonian that captures the first order Rashba effect in 2D semiconductors systems is also used to describe the surface states in a 3D topological insulator[38]: $\mathcal{H}(\mathbf{k}) = h_0(\mathbf{k}) + h_{R_1}(\mathbf{k})$. The first term $h_0(\mathbf{k}) = \xi \mathbf{k}^2$ is the quasi-free electron approximation and the second term $h_{R_1}(\mathbf{k}) = \alpha_{R_1}(\boldsymbol{\sigma} \times \mathbf{k}) \cdot \hat{z}$ represents the interaction between the spin Pauli matrices vector $\boldsymbol{\sigma}$ and the momentum \mathbf{k} . Here α_{R_1} is the Rashba coefficient, and z the unit vector perpendicular to the plane in which lies the semiconductor. When the term ξ , which depends on the effective mass m^* and the electron mass m_e ($\xi = \frac{\hbar^2}{2m^*m_e}$), is sufficiently small relative to parameter α_R , states with linear dispersion and helical spin texture appears, describing the surface states in a 3D TI. Otherwise, the Rashba effect band dispersion appears. Since $|1/2, \pm 1/2\rangle$ effective states are those that form the valence band, in which the M-shape of the Rashba effect occurs, only these states have the $h_{R_1}(\mathbf{k})$ term. Obviously both the $|1/2, \pm 1/2\rangle$ as the $|3/2, \pm 3/2\rangle$ effective states have the $h_0(\mathbf{k})$ term, which introduces the band parabolic effect. The hexagonal warping on all bands is introduced considering the three order Rashba term $h_{R_3}(\mathbf{k}) = \alpha_{R_3}[(k_x + ik_y)^3 + (k_x - ik_y)^3]\sigma_z$ [37]. Join-

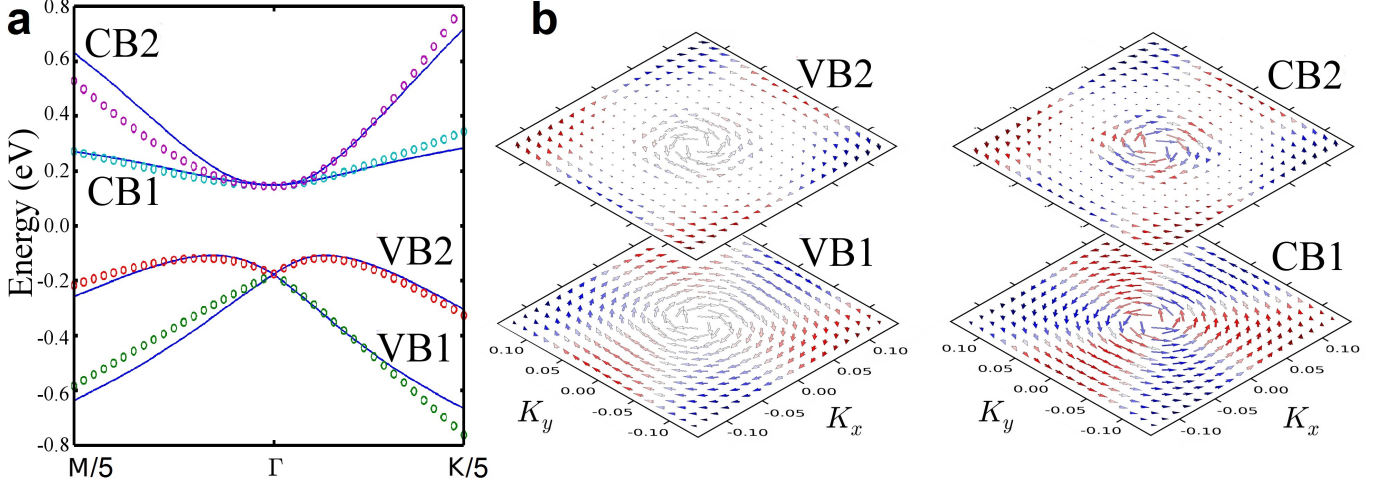


Figure 5. In (a) we have the band structure from the DFT approach (blue lines) and the effective tight binding model (circles). In (b) we calculated the spin component extracted from the model. The values for each variable of the model is given in the table I (see methods).

ing these terms, the effective Hamiltonian can be written as:

$$\mathcal{H} = \begin{pmatrix} \mathcal{H}_{1/2}(\mathbf{k}) & \mathcal{H}_{int}(\mathbf{k}) \\ \mathcal{H}_{int}^\dagger(\mathbf{k}) & \mathcal{H}_{3/2}(\mathbf{k}) \end{pmatrix}, \quad (1)$$

where $\mathcal{H}_{1/2}(\mathbf{k}) = h_0^{1/2}(\mathbf{k}) + h_{R_3}^{1/2}(\mathbf{k}) + h_{R_1}^{1/2}(\mathbf{k})$ and $\mathcal{H}_{3/2}(\mathbf{k}) = -h_0^{3/2}(\mathbf{k}) + h_{R_3}^{3/2}(\mathbf{k})$ are the effective Hamiltonian that described the $|1/2, \pm 1/2\rangle$ and $|3/2, \pm 3/2\rangle$ effective states, respectively. The phenomenological analysis of the behavior of the band structure does not provide information on the interaction Hamiltonian between these states, $\mathcal{H}_{int}(\mathbf{k})$. Therefore, we propose a fuller analysis through a tight-binding effective model. The tight-binding Hamiltonian matrix elements in the momentum space is written as,

$$H(\mathbf{k}) = \varepsilon(\mathbf{k}) + \sum_{\langle j=1 \rangle}^6 t_{\mathbf{a}_i} e^{i\mathbf{k} \cdot \mathbf{a}_i}, \quad (2)$$

where $t_{\mathbf{n}_i} = \langle \mathbf{n}, J, j_z | H | \mathbf{a}_i, J', j'_z \rangle$ is the nearest neighbor hopping term, with \mathbf{n} indicating the lattice site and \mathbf{a}_i corresponds to the i -th of the six nearest neighbor vector. Since the $|(Pb-I)_J, j_z\rangle$ effective states are not considered, we omit the terms associated with the near neighbors. Based on the symmetry properties of the system, the hopping terms can be uniquely determined. We study the behavior of the tight-binding Hamiltonian matrix elements in the $\mathbf{k} \rightarrow \Gamma$ limit, obtaining the most simplified model. From this model we have the relations between the ξ , α_{R_1} and α_{R_3} parameters and the hopping terms and the \mathcal{H}_{int} interaction term (see methods), explicitly: $\xi = 3a^2 \text{Re}(t^{11})$, $\alpha_{R_1} = \frac{3}{2} \text{Im}(t^{12})$, $\alpha_{R_3} = \frac{\sqrt{3}}{2} a^3 \text{Im}(t^{11})$ and $\mathcal{H}_{int} = i\sigma_z \frac{3}{4} a \text{Re}(t^{13})(k_x + ik_y)$.

The \mathcal{H}_{int} interaction is critical to the spin polarization transfer and the induction of the helical spin texture for the band where the major contribution comes from the $|Bi_{3/2}, \pm 3/2\rangle$ effective states. Thus, the effects mentioned above together with the band inversion allow the reproduction of both band structure and spin texture obtained via DFT calculations, as shown in Fig 5. The procedure followed for this Hamiltonian is described in the methods and the optimized values were obtained via a least squares standard approach in order to match DFT calculation (See Table I).

	m_1^*	m_2^*	α_{int}	α_{R_1}	$\alpha_{R_3}^{1/2}$	$\alpha_{R_3}^{3/2}$
Values	0.3714	0.5294	3.5853i	3.0919	12	20

Table I. Values of the parameters for the effective tight binding model.

CONCLUSIONS

From ab initio calculations we made a crystalline structure analysis, a Z_2 topological evaluation and a mapping of topological edge states. The Rashba spin splitting reported here is up to 60 meV without strain, and rise up to 90 meV with strain, providing to this system a giant Rashba effect. We also noticed an exotic spin texture with spin flipping, an unconventional effect in the Rashba splitting where, at constant energy planes in the same band index, we have two circular spin helicity turning in opposite ways, an effect of interest in spintronic devices. We also concluded that PbBiI is a topological insulator via the approach of the switching of Wanniers Centers

of Charges. This material is strong upon strain, maintaining the topological properties even for a tension of 20%, although compression may leave the material in a semi metal electronic phase. We mapped the topological edge states with opposite spin as expected from TRS, not perfectly degenerate at the inversion point, i.e Γ , due to the lack of inversion symmetry. Our finding may enable further research in this new topological material, which present such unusual spin texture.

METHODS

DFT calculations: The first-principles calculations were performed within the Density Functional Theory (DFT) framework, as implemented in the SIESTA code[44], considering the on-site approximation for the spin-orbit coupling[45]. The Local Density Approximation (LDA)[46] is used for the exchange-correlation functional. We used an energy cutoff of 410 Ry to define the grid in the real space, and the supercell approximation with a k-points sampling for the reciprocal space integration equivalent to $20 \times 20 \times 1$ in the unitary cell. The 2D PbBiI sheets lie in the xy plane, and a vacuum of 20\AA was used in the z-direction to avoid the undesirable interaction between the periodic images of PbBiI sheets. The system geometry was fully relaxed until the residual forces on the atoms were smaller than 0.01 eV/\AA .

Z_2 invariant calculation: The easiest way of discovering new topological materials is the evaluation of an invariant number always associated with a particular symmetry. For systems protected by Time Reversal (TR) symmetry, the invariant characterizing the system is called a Z_2 invariant. When this number is not zero, the system has TR protected metallic edge states.

The formulation of the Z_2 number follows many different formulations: via the parity eigenvalues for systems with inversion symmetry [47], the formulation via Resta polarization [42], by an integration of the Berry phase over the effective Brillouin zone [40], and by the switching of Wannier Center of Charges (WCCs)[43]. When the materials are non-centrosymmetric, the *ab initio* calculations can give a generic gauge [43] on the states. Therefore, we chose to calculate the Z_2 invariant via the switching of WCCs. In that manner, we know that the Z_2 invariant can be written as:

$$Z_2 = P_{\Theta}(t = T/2) - P_{\Theta}(t = 0), \quad (3)$$

where t represents an adiabatic time. Now we want to rewrite equation (3) in terms of the WCCs. For that, we need to define Wannier functions (WF). The WFFs belonging the the same unit cell R have the following

format:

$$|Rn\rangle = \frac{1}{2\pi} \int_{-\pi}^{\pi} dk e^{-ik(R-x)} |u_{nk}\rangle. \quad (4)$$

A WCC \bar{x}_n is defined as the mean value of $\langle 0n|\hat{X}|0n\rangle$ where \hat{X} is the position operator and $|0n\rangle$ is the state corresponding to a WF in the cell with $R = 0$. So we have:

$$\bar{x}_n = \frac{i}{2\pi} \int_{-\pi}^{\pi} dk \langle u_{nk} | \partial_k | u_{nk} \rangle. \quad (5)$$

Assuming that we got $\sum_{\alpha} \bar{x}_{\alpha}^S = \frac{1}{2\pi} \oint_{BZ} A^S$ with $S = I, II$, where sumation in α represents occupied states and A the Berry connection, we finally have:

$$Z_2 = \sum_{\alpha} [\bar{x}_{\alpha}^I(T/2) - \bar{x}_{\alpha}^{II}(T/2)] - \sum_{\alpha} [\bar{x}_{\alpha}^I(0) - \bar{x}_{\alpha}^{II}(0)]. \quad (6)$$

With the smooth gauge condition between $t \in [0, T/2]$ it is possible to track the evolution of WCCs during a half cycle, which is also smooth. It is important to note that this argumentation is only valid when some properties are valid for the construction of the Wannier Functions. Now if we have an even or odd number of crossing between half cycle of the WCCs, we are dealing with a trivial or a topological material, i.e Z_2 equal 0 or 1.

ACKNOWLEDGEMENTS

We would like to thank the financial support by the Fundação de Amparo à Pesquisa do Estado de São Paulo (FAPESP) and Conselho Nacional de Desenvolvimento Científico e Tecnológico/Institutos Nacionais de Ciência e Tecnologia do Brasil (CNPq/INCT). Thanks to Gina Polo and Sylvia Mueni for the linguistic support.

AUTHOR CONTRIBUTIONS

CMA and OB performed the first principle calculation and developed the effective Hamiltonian model. LBA did the Z_2 calculations. AF supervised the project. CMA wrote the manuscript with contributions from all authors. All authors equally discussed the results and contributed to the understanding.

* acosta@if.usp.br

† fazzio@if.usp.br

[1] D. Pesin and A. H. MacDonald, Nat Mater **11**, 409 (2012).

[2] I. Žutić, J. Fabian, and S. Das Sarma, Rev. Mod. Phys. **76**, 323 (2004).

- [3] A. Brataas, A. D. Kent, and H. Ohno, *Nat Mater* **11**, 372 (2012).
- [4] T. Liang, Q. Gibson, M. N. Ali, M. Liu, R. J. Cava, and N. P. Ong, *Nat Mater* **14**, 280 (2015), letter.
- [5] L. Liu, O. J. Lee, T. J. Gudmundsen, D. C. Ralph, and R. A. Buhrman, *Phys. Rev. Lett.* **109**, 096602 (2012).
- [6] M. Z. Hasan and C. L. Kane, *Rev. Mod. Phys.* **82**, 3045 (2010).
- [7] X.-L. Qi and S.-C. Zhang, *Rev. Mod. Phys.* **83**, 1057 (2011).
- [8] L. V. Kulik, A. V. Gorbunov, A. S. Zhuravlev, V. B. Timofeev, S. Dickmann, and I. V. Kukushkin, *Sci. Rep.* **5** (2015), article.
- [9] S. Maekawa, S. O. Valenzuela, E. Saitoh, and T. Kimura, *Spin Current* (Series on Semiconductor Science and Technology 17, Oxford University Press, 2012).
- [10] R. Jansen, *Nat Mater* **11**, 400 (2012).
- [11] L. Liu, C.-F. Pai, Y. Li, H. W. Tseng, D. C. Ralph, and R. A. Buhrman, *Science* **336**, 555 (2012), <http://www.sciencemag.org/content/336/6081/555.full.pdf>.
- [12] Ishizaka K., Bahramy M. S., Murakawa H., Sakano M., Shimojima T., Sonobe T., Koizumi K., Shin S., Miyahara H., Kimura A., Miyamoto K., Okuda T., Namatame H., Taniguchi M., Arita R., Nagaosa N., Kobayashi K., Murakami Y., Kumai R., Kaneko Y., Onose Y., and Tokura Y., *Nat Mater* **10**, 521526 (2011), 10.1038/nmat3051.
- [13] Bahramy M.S., Yang B.-J., Arita R., and Nagaosa N., *Nat Commun* **3**, 679 (2012), 10.1038/ncomms1679.
- [14] L. Barreto, L. Khnemund, F. Edler, C. Tegenkamp, J. Mi, M. Bremholm, B. B. Iversen, C. Frydendahl, M. Bianchi, and P. Hofmann, *Nano Letters* **14**, 3755 (2014), pMID: 24940641, <http://dx.doi.org/10.1021/nl501489m>.
- [15] Y. A. Bychkov and E. I. Rashba, *JETP Lett* **39**, 78 (1984).
- [16] S. LaShell, B. A. McDougall, and E. Jensen, *Phys. Rev. Lett.* **77**, 3419 (1996).
- [17] C. R. Ast, J. Henk, A. Ernst, L. Moreschini, M. C. Falub, D. Pacilé, P. Bruno, K. Kern, and M. Grioni, *Phys. Rev. Lett.* **98**, 186807 (2007).
- [18] Y. M. Koroteev, G. Bihlmayer, J. E. Gayone, E. V. Chulkov, S. Blügel, P. M. Echenique, and P. Hofmann, *Phys. Rev. Lett.* **93**, 046403 (2004).
- [19] J. Nitta, T. Akazaki, H. Takayanagi, and T. Enoki, *Phys. Rev. Lett.* **78**, 1335 (1997).
- [20] T. Hirahara, T. Nagao, I. Matsuda, G. Bihlmayer, E. V. Chulkov, Y. M. Koroteev, P. M. Echenique, M. Saito, and S. Hasegawa, *Phys. Rev. Lett.* **97**, 146803 (2006).
- [21] S. Mathias, A. Ruffing, F. Deicke, M. Wiesenmayer, I. Sakar, G. Bihlmayer, E. V. Chulkov, Y. M. Koroteev, P. M. Echenique, M. Bauer, and M. Aeschlimann, *Phys. Rev. Lett.* **104**, 066802 (2010).
- [22] H. Yuan, M. S. Bahramy, K. Morimoto, S. Wu, K. Nomura, B.-J. Yang, H. Shimotani, R. Suzuki, M. Toh, C. Kloc, X. Xu, R. Arita, N. Nagaosa, and Y. Iwasa, *Nat Phys* **9**, 563 (2013), article.
- [23] J. H. Dil, F. Meier, J. Lobo-Checa, L. Patthey, G. Bihlmayer, and J. Osterwalder, *Phys. Rev. Lett.* **101**, 266802 (2008).
- [24] C. L. Kane and E. J. Mele, *Phys. Rev. Lett.* **95**, 146802 (2005).
- [25] S. Cahangirov, M. Topsakal, E. Aktürk, H. Şahin, and S. Ciraci, *Phys. Rev. Lett.* **102**, 236804 (2009).
- [26] W.-F. Tsai, C.-Y. Huang, T.-R. Chang, H. Lin, H.-T. Jeng, and A. Bansil, *Nat Commun* **4**, 1500 (2013).
- [27] P. Vogt, P. De Padova, C. Quaresima, J. Avila, E. Frantzeskakis, M. C. Asensio, A. Resta, B. Ealet, and G. Le Lay, *Phys. Rev. Lett.* **108**, 155501 (2012).
- [28] Y. Xu, B. Yan, H.-J. Zhang, J. Wang, G. Xu, P. Tang, W. Duan, and S.-C. Zhang, *Phys. Rev. Lett.* **111**, 136804 (2013).
- [29] L. Song, L. Ci, H. Lu, P. B. Sorokin, C. Jin, J. Ni, A. G. Kvashnin, D. G. Kvashnin, J. Lou, B. I. Yakobson, and P. M. Ajayan, *Nano Letters* **10**, 3209 (2010), pMID: 20698639, <http://dx.doi.org/10.1021/nl1022139>.
- [30] W. Lei, D. Portehault, D. Liu, S. Qin, and Y. Chen, *Nat Commun* **4**, 1777 (2013), article.
- [31] RadisavljevicB., RadenovicA., BrivioJ., GiacomettiV., and KisA., *Nat Nano* **6**, 147 (2011).
- [32] S. Z. Butler, S. M. Hollen, L. Cao, Y. Cui, J. A. Gupta, H. R. Gutierrez, T. F. Heinz, S. S. Hong, J. Huang, A. F. Ismach, E. Johnston-Halperin, M. Kuno, V. V. Plashnitsa, R. D. Robinson, R. S. Ruoff, S. Salahuddin, J. Shan, L. Shi, M. G. Spencer, M. Terrones, W. Windl, and J. E. Goldberger, *ACS Nano* **7**, 2898 (2013), pMID: 23464873, <http://dx.doi.org/10.1021/nn400280c>.
- [33] C. Si, J. Liu, Y. Xu, J. Wu, B.-L. Gu, and W. Duan, *Phys. Rev. B* **89**, 115429 (2014).
- [34] C.-X. Liu, X.-L. Qi, H. Zhang, X. Dai, Z. Fang, and S.-C. Zhang, *Phys. Rev. B* **82**, 045122 (2010).
- [35] K. Ishizaka, M. S. Bahramy, H. Murakawa, M. Sakano, T. Shimojima, T. Sonobe, K. Koizumi, S. Shin, H. Miyahara, A. Kimura, K. Miyamoto, T. Okuda, H. Namatame, M. Taniguchi, R. Arita, N. Nagaosa, K. Kobayashi, Y. Murakami, R. Kumai, Y. Kaneko, Y. Onose, and Y. Tokura, *Nat Mater* **10**, 521 (2011).
- [36] L. Fu, *Phys. Rev. Lett.* **103**, 266801 (2009).
- [37] S. Vajna, E. Simon, A. Szilva, K. Palotas, B. Ujfalussy, and L. Szunyogh, *Phys. Rev. B* **85**, 075404 (2012).
- [38] E. Frantzeskakis and M. Grioni, *Phys. Rev. B* **84**, 155453 (2011).
- [39] Z. B. Siu, M. B. A. Jalil, and S. G. Tan, *Sci. Rep.* **4** (2014), article.
- [40] T. Fukui, T. Fujiwara, and Y. Hatsugai, *Journal of the Physical Society of Japan* **77**, 123705 (2008), <http://dx.doi.org/10.1143/JPSJ.77.123705>.
- [41] J. E. Moore and L. Balents, *Phys. Rev. B* **75**, 121306 (2007).
- [42] L. Fu and C. L. Kane, *Phys. Rev. B* **74**, 195312 (2006).
- [43] R. Yu, X. L. Qi, A. Bernevig, Z. Fang, and X. Dai, *Phys. Rev. B* **84**, 075119 (2011).
- [44] J. M. Soler, E. Artacho, J. D. Gale, A. García, J. Junquera, P. Ordejón, and D. Sánchez-Portal, *Journal of Physics: Condensed Matter* **14**, 2745 (2002).
- [45] C. M. Acosta, M. P. Lima, R. H. Miwa, A. J. R. da Silva, and A. Fazzio, *Phys. Rev. B* **89**, 155438 (2014).
- [46] J. P. Perdew and A. Zunger, *Phys. Rev. B* **23**, 5048 (1981).
- [47] L. Fu and C. L. Kane, *Phys. Rev. B* **76**, 045302 (2007).